Energy & Environmental Science

Methanol Tolerance of Atomically Dispersed Single Metal Site Catalysts: Mechanistic Understanding and High-performance Direct Methanol Fuel Cells

Journal:	*Energy & Environmental Science*
Manuscript ID	EE-ART-06-2020-001968.R1
Article Type:	Paper
Date Submitted by the Author:	03-Aug-2020

Complete List of Authors:	Shi, Qiurong ; University at Buffalo - The State University of New York, Chemical and Biological Engineering He, Yanghua; University at Buffalo - The State University of New York, Chemical and Biological Engineering Bai, Xiaowan; University of Texas at Austin Wang , Maoyu; Oregon State University, School of Chemical, Biological, and Environmental Engineering Cullen, David; Oak Ridge National Laboratory, Materials Science & Technology Division Lucero, Marcos ; Oregon State University, School of Chemical, Biological, and Environmental Engineering Zhao, Xunhua; University of Texas System, Physics More, Karren; Oak Ridge National Laboratory, Center for Nanophase Materials Sciences Zhou, Hua; Argonne National Laboratory, Advanced Photon Source Feng, Zhenxing; Oregon State University, School of Chemical, Biological, and Environmental Engineering; Liu, Yuanyue; University of Texas at Austin Wu, Gang; University at Buffalo - The State University of New York, Chemical and Biological Engineering

ARTICLE

Methanol Tolerance of Atomically Dispersed Single Metal Site Catalysts: Mechanistic Understanding and High-performance Direct Methanol Fuel Cells

Received 00th January 20xx,
Accepted 00th January 20xx

DOI: 10.1039/x0xx00000x

Qiurong Shi,[a,1] Yanghua He,[a,1] Xiaowan Bai[b,1], Maoyu Wang[c], David A. Cullen[d], Macros Lucero[c], Xunhua Zhao[b], Karren L. More[d], Hua Zhou[e], Zhenxing Feng[c]*, Yuanyue Liu[b]* and Gang Wu[a]*

Abstract: Proton-exchange membrane fuel cells (PEMFCs) and direct methanol fuel cells (DMFCs) are promising power sources from portable electronic devices to vehicles. The high-cost issue of these low-temperature fuel cells can be primarily addressed by using platinum-group metal (PGM)-free oxygen reduction reaction (ORR) catalysts, in particular atomically dispersed metal-nitrogen-carbon (M-N-C, M=Fe, Co, Mn). Furthermore, a significant advantage of M-N-C catalysts is their superior methanol tolerance over Pt, which can mitigate the methanol cross-over effect and offer a great potential of using a higher concentration of methanol in DMFCs. Here, we investigated the ORR catalytic behaviors of M-N-C catalysts in methanol-containing acidic electrolytes via experimental and density functional theory (DFT) calculation. FeN_4 sites demonstrated the highest methanol tolerance ability when compared to metal-free pyridinc N, CoN_4, and MnN_4 active sites. The methanol adsorption on MN_4 sites is even strengthened when electrode potentials are applied during the ORR. The negative influence of methanol adsorption becomes significant when methanol concentrations are higher than 2.0 M. However, the methanol adsorption does not affect the $4e^-$ ORR pathway and chemically destroys the FeN_4 sites. The understanding of methanol-induced ORR activity loss guides to design the promising M-N-C cathode catalyst in DMFCs. Accordingly, we developed a dual-metal site Fe/Co-N-C catalyst through a combined chemical-doping and adsorption strategy. Instead of generating the synergistic effect, introducing Co atoms in the first doping step acts as "scissors" for Zn removal in metal-organic frameworks (MOFs), which is crucial for modifying the porosity of the catalyst and providing more defects for stabilizing the active FeN_4 sites generated in the second adsorption step. The Fe/Co-N-C catalyst significantly improved the ORR catalytic activity and delivered remarkably enhanced peak power densities (*i.e.*, 502 and 135 mW cm^{-2}) under H_2-air and methanol-air conditions, respectively, representing the best performance for both types of fuel cells. Notably, the fundamental understanding of methanol tolerance, along with the encouraging DMFC performance, will open an avenue for the potential application of atomically dispersed M-N-C catalysts in other direct alcohol fuel cells.

Introduction

Currently, the global environmental pollution issues and fossil fuel crisis have been increasingly exacerbated. This intrigued extensive researches on developing sustainable and renewable electrochemical energy conversion technologies, including proton-exchange membrane fuel cells (PEMFCs), direct methanol fuel cell (DMFC), and water electrolyzers.[1-4] Numerous efforts have been devoted to the study of PEMFCs due to their relatively high efficiency and environmental-benign properties for applications majorly in electric vehicles. Alternatively, DMFCs is attractive for applications of portable electronics due to their high energy density and easy storage/transport of methanol.[5-9] In both PEMFCs and DMFCs, the advancement of the oxygen reduction reaction (ORR) cathode catalysts is vitally crucial for promoting their overall performance. For the state-of-the-art Pt catalysts, the exorbitant cost, insufficient durability, and the inferior methanol/impurity tolerance largely rendered the wide applications of fuel cells.[10] Recently, platinum group metal-free (PGM-free) catalysts, especially the atomically dispersed M-N-C (M=Fe, Co, Mn) material, have exhibited encouraging activity and stability in acidic media, holding a great promise as ORR cathode catalysts.[6, 11-21] Importantly, the methanol tolerance of M-N-C catalysts endows them another advantageous feature for DMFCs.[6, 9, 22-25] It has long been denounced that the serious methanol cross-over from anode to cathode resulted in the significant performance loss at the Pt/C cathode, remaining a significant factor in inefficiencies of DMFCs. The methanol cross-over dramatically reduces the overall cell voltages due to a mixed potential generated from simultaneous ORR and methanol oxidation

[a] *Department of Chemical and Biological Engineering, University at Buffalo, The State University of New York, Buffalo, NY 14260, USA. E-mail: gangwu@buffalo.edu*
[b] *Texas Materials Institute and Department of Mechanical Engineering, The University of Texas at Austin, Austin, Texas 78712, USA. E-mail: Yuanyue.liu@austin.utexas.edu*
[c] *School of Chemical Biological, and Environmental Engineering Oregon State University, Corvallis, OR 97331, USA. E-mail: Zhenxing.feng@oregonstate.edu*
[d] *Center for Nanophase Materials Sciences, Oak Ridge National Laboratory, Oak Ridge National Laboratory, Oak Ridge, TN 37831, USA*
[e] *X-ray Science Division, Argonne National Laboratory, Lemont, IL, 60439, USA.*
*Corresponding authors
[1] These authors contributed equally.

Electronic Supplementary Information (ESI) available: See DOI: 10.1039/x0xx00000x

reaction (MOR). Methanol also poisons Pt sites and inhibits catalytic performance at the cathode. The cross-over becomes aggravated with an increase of methanol concentration, which impedes the use of methanol with high concentrations for achieving high-power DMFCs.

Among studied M-N-C catalysts,[12, 26, 27] Fe-N-C materials, consisting of FeN_4 active sites embedded into carbon planes, demonstrated the best activity toward ORR catalysis in acidic electrolytes.[8, 9, 14, 15, 28, 29] Tremendous efforts have been focusing on the modifications of the local coordination environment and atomic structure of active sites and the overall morphology of catalysts for enhancing performance and durability. [12, 18, 28, 30-33] Nevertheless, membrane electrode assembly (MEA) performances of current Fe-N-C cathodes under H_2-air conditions are still insufficient, including power density and durability. Alternatively, the potential application of M-N-C catalysts in DMFCs is more attractive.[34, 35] Due to kinetically slow methanol oxidation at the anode, the M-N-C cathode can easily generate sufficient current density to match. Therefore, the relatively low performance of M-N-C cathodes is not the major limitation in DMFCs. Many groups, including us, have made a significant contribution to engineering the PGM anode and the Fe-N-C cathode in boosting the performances of DMFCs.[6, 8, 9, 22] However, the power density of the methanol-air cell is still far away from the U.S. DOE's target of 250 mW cm^{-2}. Besides, fundamental studies on M-N-C catalysts in terms of their methanol tolerance capability, methanol adsorption on active sites, and methanol cross-over effect in MEA performance still lack in the field, which is of great importance in guiding the rational design of M-N-C catalysts for DMFC applications.

Here, we conducted fundamental studies using a well-defined atomically dispersed Fe-N-C catalyst, exclusively containing FeN_4 active sites,[36] which aims to convey a cognition toward the methanol-induced ORR catalytic behavior. Combined with theoretical study, we revealed that FeN_4 sites exhibited the weakest methanol adsorption ability among pyridinc N, CoN_4, and MnN_4 sites, which validated its exceptional advantage for DMFCs. The adsorption on MN_4 sites is involved with the electrochemical process and is strengthened when potentials are applied for the ORR. However, the methanol adsorption does not affect the $4e^-$ ORR pathway and damage the structure of the FeN_4 site. Based on the understanding, we accordingly designed and synthesized an atomically dispersed dual-site Fe/Co-N-C catalyst via an innovative two-step chemical-doping and adsorption strategy, demonstrating improved catalytic performance and mass transport in DMFCs. Compared to conventional single metal sites, a dual-metal site may provide a new opportunity to design innovative M-N-C catalysts with enhanced intrinsic activity and stability due to optimal modifications of local geometric and electronic structures.[37] Wang *et.al* have reported a dual-site (Fe, Co)-N-C catalyst to enhance the intrinsic activity of FeN_x sites through a synergistic effect.[38] In contrast, in our work, instead of generating the synergistic effect, the doping of Co species in the first step act as "scissors" for Zn removal during the carbonization of zeolitic imidazolate framework-8 (ZIF-8) precursors to create more defects, which is crucial for generating FeN_4 active sites in the second adsorption step with favorable porosity. The Fe/Co-N-C catalyst yielded promising intrinsic ORR activity in acidic electrolytes with a half-wave potential ($E_{1/2}$) of 0.85 V *vs.* RHE. Importantly, in MEAs, it demonstrated the ever record power density of 502 and 135 mW cm^{-2} in H_2- and methanol-air cells, respectively, representing the best performance so far for both types of fuel cells.

Results and discussion

Mechanistic studies of ORR in the presence of methanol.

We employed a Fe-N-C catalyst exclusively containing FeN_4 active site as an ideal model to study the effect of methanol concentration on the ORR in acidic electrolytes. As shown in the high-angle annular dark-field scanning electron microscopy (HAADF-SEM) and scanning transmission electron microscopy (STEM) image (**Fig. S1**), the Fe-N-C catalyst is featured with typical atomic dispersed single Fe sites and displayed a uniform carbon particle size distribution of about 65 nm. Importantly, its sufficient ORR catalytic activity and stability (**Fig. S2**), are perfect for the fundamental studies of methanol tolerance of FeN_4 active sites.

The Fe-N-C catalyst exhibited negligible activity changes (*i.e.*, 3 mV in $E_{1/2}$ shift) when methanol concentration is below 2.0 M in O_2-saturated 0.5 M H_2SO_4 electrolyte (**Fig. 1**A). However, when the methanol concentration is over 2.0 M, it showed noticeable activity degradation. The activity could not be recovered by transferring the RDE working electrode from methanol-containing electrolyte back to the methanol-free one (**Fig. 1**B-C and **Fig. S3**). This suggests that methanol could be firmly adsorbed on the FeN_4 active site and affect ORR activity. Oppositely, the presence of methanol promotes O_2 solubility and diffusion in electrolytes. For example, when the methanol concentration reached to 16.0 M (**Fig. S3**C), the diffusion limiting current increased sharply. That is partially caused by the significant changes in the O_2 diffusion coefficient and the solubility in the electrolyte containing a high concentration of methanol.[39, 40] Regardless with or without methanol, the ORR on FeN_4 sites still follows the 4 electron pathway with negligible H_2O_2 yields (**Fig. 1**D). It indicates that the presence of methanol does not change the ORR catalysis pathway or damage the structure of FeN_4 sites.[41] To further prove that most of the FeN_4 sites are free and remain intact, we further added the KSCN to the methanol-free H_2SO_4 electrolyte by using the Fe-N-C catalyst that was already degraded in the methanol-containing electrolyte. We found that the ORR activity suffered from a severe degradation (**Fig. S4**A), which is similar to the $E_{1/2}$ decay when the fresh Fe-N-C catalyst was directly tested in KSCN-containing electrolyte (**Fig. S**4B). That means that the methanol adsorption on the FeN_4 site is not strong enough to block SCN^- ions. The poisoning of SCN^- ions to FeN_4 sites easily causes significant activity loss for the ORR.

ARTICLE

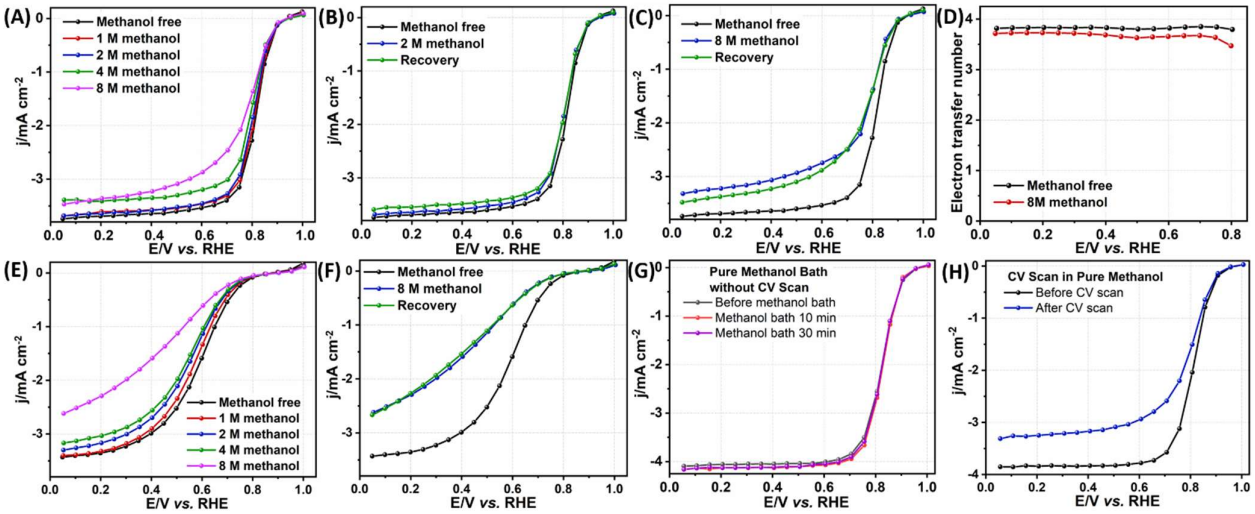

Fig. 1. ORR polarization plots of the Fe-N-C catalysts in O_2 saturated 0.5 M H_2SO_4 aqueous solution containing different methanol concentrations (A) and their selected rinse recovery polarization plots obtained by transferring the electrode back in a methanol-free electrolyte (B and C) with a rotating rate of 900 rpm. (D) Electron transfer number of Fe-N-C catalysts in O_2-saturated 0.5 M H_2SO_4 electrolyte without and within 8 M methanol, respectively. ORR polarization plots of the ZIF-8-derived N-C catalysts in O_2-saturated 0.5 M H_2SO_4 aqueous solution containing different methanol concentrations (E) and the selected recovery in methanol-free O_2-saturated 0.5 M H_2SO_4 electrolyte (F) with a rotating rate of 900 rpm. ORR polarization plots of the Fe-N-C catalysts in O_2 saturated 0.5 M H_2SO_4 with rotating speed of 900 rpm (G) after pure methanol bath without CV scan and (H) after pure methanol bath with CV scan (0-1.0 V, 20 cycles).

Fe-N-C catalysts usually contain two types of active sites for ORR electrocatalysis: FeN_4 moieties and metal-free pyridinic N.[42] To discriminate the likely methanol adsorption sites, the methanol tolerance study was also conducted by using a ZIF-8 derived N-C catalyst, which majorly contains dominant pyridinic N dopants. The N-C catalyst exhibited significant activity loss, *i*.e., 21 mV and 37 mV negative shifts of $E_{1/2}$, much higher than that of Fe-N-C in acidic electrolytes with 1.0 and 2.0 M methanol, respectively (**Fig. 1**E). Thus, methanol is more easily to be adsorbed onto pyridinic N sites than FeN_4 sites. After the metal-free N-C catalyst was transferred from methanol-containing electrolyte back to a methanol-free one, the ORR polarization plots showed no recovery regardless of methanol concentrations (**Fig.** 1F and **Fig. S5**). Therefore, pyridinic N sites possess a stronger methanol adsorption ability and induce a much sever activity decay when compared to FeN_4 active sites in Fe-N-C catalysts.

To mitigate methanol-induced activity decay, we conducted a series of electrochemical tests for investigating the methanol adsorption processes. The Fe-N-C catalyst was first immersed into pure methanol for 10 and 30 mins, respectively, followed by being transferred back to methanol-free 0.5 M H_2SO_4 electrolyte. The ORR polarization plots were almost overlapped with the one without methanol adsorption (**Fig. 1**G). This is different from the KSCN poisoning studies (**Fig. S6**), implying that methanol could not be adsorbed onto the catalysts through the chemical adsorption. Oppositely, when the potential cycles (0-1.0 V *vs.* RHE for 20 cycles) were applied in pure methanol electrolyte, the behavior is different. Compared to the Fe-N-C catalyst in fresh 0.5 M H_2SO_4, the catalyst, which is subject to potential cycling in methanol solution, exhibited a significant negative shift of the $E_{1/2}$ along with limiting current decay (**Fig. 1H**). This phenomenon evidenced that the adsorption of methanol on FeN_4 sites involved with the electrochemical process, rather than the traditional chemical or electrostatic interactions. When the Fe-N-C catalyst transferred back to methanol free-electrolyte), it was challenging to remove the adsorbed methanol through simple rinsing with a methanol-free solution (**Fig. 1B** and C).

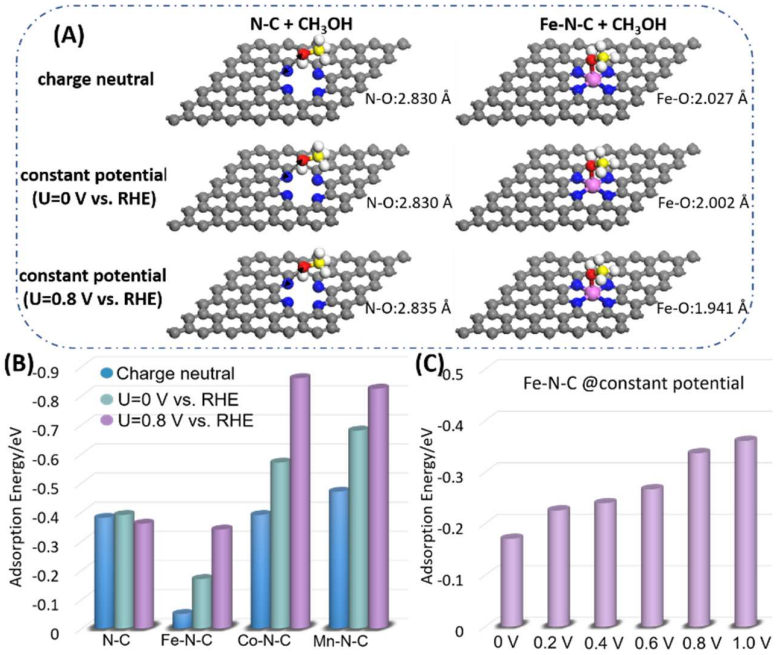

Fig. 2. (A) Adsorption mode of CH_3OH on the N-C and Fe-N-C catalysts as obtained using DFT with Perdew–Burke–Ernzerhof functional. (B) The adsorption energy of CH_3OH on the N-C, Fe-N-C, Co-N-C, and Mn-N-C catalysts, calculated using the charge-neutral method and constant potential method at U =0 and 0.8 V *vs.* RHE, respectively. (C) The adsorption energy of CH_3OH as a function of the applied potential for the Fe-N-C catalyst.

However, after we tried a drying treatment at 30°C under vacuum to remove methanol, ORR activity of the catalyst was nearly recovered (**Fig. S7**), which was not observed by merely rinsing with a methanol-free solution. This suggests that FeN_4 sites remain intact after completely removing methanol. The methanol tolerance of Co-N-C and Mn-N-C catalysts,[13, 18] were also studied in 0.5 M H_2SO_4 electrolyte containing different methanol concentrations, as depicted in **Fig. S8**A and S8B, respectively. Fe-N-C catalysts exhibited higher methanol tolerance than that of Co-N-C and Mn-N-C catalysts, as they displayed 3, 15, and 12 mV negative shifts of $E_{1/2}$ in an electrolyte with 1.0 M methanol, respectively.

Density functional theory (DFT) calculations were conducted to elucidate further the methanol adsorption behavior on different active sites, including pyridinic N-C and MN_4 (M=Fe, Co, and Mn). **Fig.** 2A illuminates the most stable adsorption modes of methanol molecule on pyridinic N and FeN_4 sites under charge-neutral and applied constant potential conditions (U=0 and 0.8 V *vs*. RHE), respectively. The methanol adsorption modes on CoN_4 and MnN_4 catalysts are also displayed in **Fig. S9**. As shown in **Fig. 2**B, FeN_4 sites have the smallest adsorption energy among the four studied ones under both the charge-neutral and at constant applied potential, implying that FeN_4 active sites possess the highest methanol tolerance ability. This theoretical prediction agrees with the above-mentioned experimental results that FeN_4 sites presented the highest methanol resistance ability than pyridinic N, CoN_4, and MnN_4 sites. As the constant potential method is applied on the active sites,[43-45] the adsorption energy of MN_4 sites increases. Oppositely, for the N-C sites, the adsorption energy keeps unchanged. This indicates that the applied potential could facilitate the methanol adsorption on MN_4 sites. The higher the applied potential, the stronger the methanol adsorption on the FeN_4 site (**Fig. 2**C), but still lower than the other three types of active sites. The reason why the M-N-C catalysts are more sensitive to the potential than the N-C catalysts is that methanol is closer to M-N-C than to N-C. As shown in Fig. 2a and Fig. S10, the distance from the O atom in methanol is ~2.8 Å to the nearest N atom in N-C, while ~2.0 Å to the metal atom in M-N-C. Taking the Fe-N-C catalyst as an example, **Fig. S10** shows that with increasing potential, the Fermi level gradually downshifts with respect to the characteristic peaks of the Fe 3d orbital. This change in electronic states occupation alters the orbital hybridization between the metal atom and the bonded O atom in M-N-C system, thereby changing the adsorption energy.[43-45] In contrast, for N-C, the methanol is too far. Thus, there is no effective orbital hybridization regardless of the potential. Hence, in this case, the adsorption energy is not sensitive to the potential. These theoretical calculations are also in accordance with the experimental results that methanol adsorption on MN_4 sites are involved with the electrochemical process rather than the chemical or electrostatic adsorption. Hence, experimental and theoretical results both suggested that the Fe-N-C catalyst has enhanced methanol tolerance capability relative to N-C and other M-N-C catalysts.

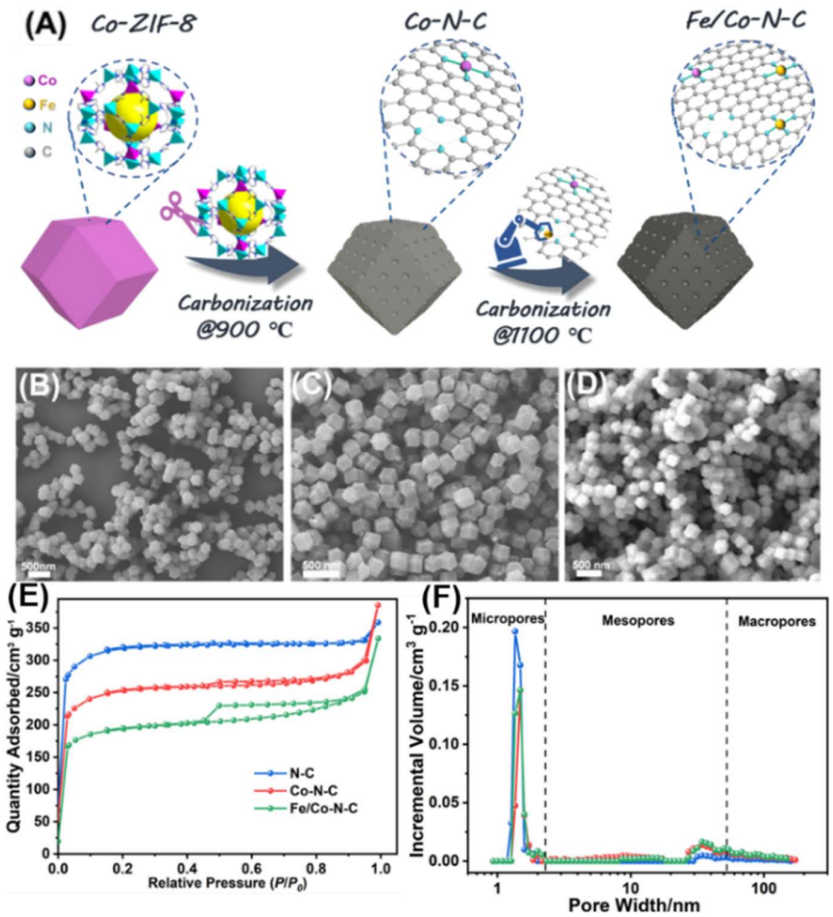

Fig. 3. (A)Schematic illustration of the Fe/Co-N-C synthesis via a two-step chemical doping and adsorption strategy. SEM images of (B) Co-doped ZIF-8, (C) Co-doped ZIF-8 derived Co-N-C and (D) Fe/Co-N-C nanocrystals. (E) Nitrogen adsorption-desorption isotherm curves and (F) pore distribution of the N-C, Co-N-C, and as-derived Fe/Co-N-C (Zn/Co=11/2) electrocatalysts, respectively.

Fe/Co-N-C catalysts design, synthesis, and characterizations.

In addition to intrinsic activity, optimizing the porosity of M-N-C catalysts is of critical importance in boosting mass activity through facilitating the mass transfer and favoring the reactants accessible to more interior active sites.[18, 33, 38, 46] Here, we design a binary metal site Fe/Co-N-C catalyst for modifying the porosity of the carbon support and increasing the density of FeN_4 active sites. The synthesis of Fe/Co-N-C catalysts contains a two-step chemical doping and adsorption procedure (**Fig. 3A**). Firstly, the Co-doped ZIF-8 crystalline precursor was prepared with a controlled Zn/Co feeding ratio, followed by pyrolysis at 900 °C for one hour.[18] As a result, a porous and atomically dispersed Co-N-C catalyst was synthesized. Then, the Co-N-C catalyst was served as the host for sequent Fe ions adsorption. The secondary pyrolysis at 1100 °C for one hour is to prepare a Fe/Co-N-C catalyst, dominantly containing FeN_4 active sites. **Fig. 3B** to **3D** exhibited the morphologies of the Co-doped ZIF-8 nanocrystal precursor, the Co-N-C, and the Fe/Co-N-C catalyst, respectively. Their particle shapes and size were well-maintained after the two-steps heating treatment, suggesting the effectiveness of achieving homogeneous catalyst morphologies by using ZIF-8 as precursors.

Due to the relatively low Co doping content, the introduction of Co does not significantly change the graphitization degree of carbon hosts (**Fig. S11**), which agrees with other similar works.[14, 18] The purpose of introducing Co is not for generating a possible synergistic effect of the dual-site catalyst to improve its intrinsic activity. Instead, the doping of Co is to modify catalyst porosity and structure. In particular, Co sites are of vital importance in acting as "scissors" in favoring the Zn removal from the ZIF-8 precursor during the first heat treatment at 900 °C and generation of significant mesopores. Compared to the ZIF-8-derived N-C, the Co-doped ZIF-8 derived Co-N-C is dominant with mesopore as evidenced from the nitrogen adsorption-desorption isotherm curves and pore distribution plots in **Fig. 3E** and **3F**). Importantly, the mesopore feature can be retained in the Fe/Co-N-C catalyst after the second adsorption and thermal activation. Meanwhile, the decreased micropore volume in the Co-N-C and Fe/Co-N-C catalysts is possibly attributed to the more efficient Zn removal facilitated by the pre-doping of Co sites. As shown in **Table S1**, the X-ray Fluorescence (XRF) analysis of the Zn and Co content indicated that pre-doping of Co sites in ZIF-8s along with the second treatment would significantly reduce the residual Zn amount in the catalysts.

ARTICLE

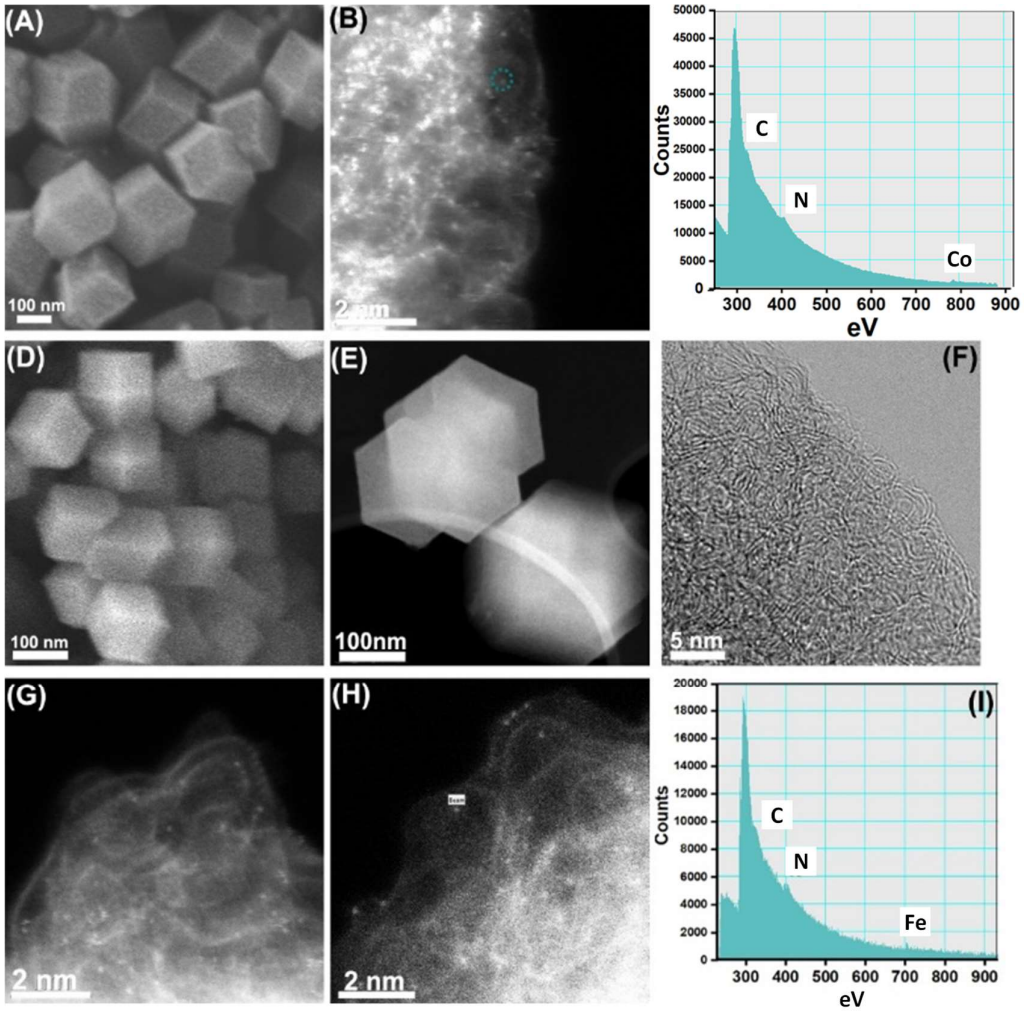

Fig. 4. (A) SEM images, (B) HAADF-STEM image, and (C) EELS analysis of Co-doped ZIF-8-derived Co-N-C catalysts. (D) SEM, (E) STEM, (F) HRTEM, (G-H) HAADF-STEM, and (I) EELS analysis of as-obtained Fe/Co-N-C catalysis.

The Zn removal promoted by the pre-doped Co is probably attributed to the accelerated decomposition of the linkage between the metal and imidazolate.[38, 47] Removing Zn atoms may benefit for creating more defects for the FeN_4 site formation because increased N-coordinated sites become available for additional Fe ions adsorption in the second heating treatment. Hence, Co-doping is crucial in modifying the porosity of the catalyst for favoring mass transfer and exposing more interior active sites accessible to reactants. The porosity modification does not change the graphitization degree of the carbon support during the first heating treatment at 900 °C. However, higher temperatures, such as 1100 °C, could promote the degree of graphitization of carbon in catalysts (**Fig. S11**).[14, 18]

The Co-N-C catalyst showed uniform size distribution of around 150-200 nm without any detectable metal clusters or nanoparticles (**Fig. 4**A). The optimized Zn/Co precursor feeding ratio (*e.g.*, 11/2) is critical for avoiding the generation of Co aggregates. Atomically dispersed single Co sites were observed from the HAADF-STEM image in **Fig. 4**B. The co-existence of Co and N at the atomic level is verified by using EELS (**Fig. 4**C), suggesting the formation of atomically dispersed and nitrogen coordinated CoN_4 sites. The coordination number was verified by using XAS, which is discussed later. The Fe/Co-N-C catalyst inherited the morphology and size distribution of the Co-N-C catalyst after the formation of FeN_4 sites (shown in **Fig. 4**D and **4**E). The surface of the Fe/Co-N-C catalysts is "clean" without any observable metal nanoclusters or particles,

indicating the well-controlled Fe adsorption content for synthesizing the atomically dispersed single metal sites without generating any inactive Fe aggregates. The bright-field STEM image in **Fig. 4**F represented the partially graphitized carbon fringes of the Fe/Co-N-C catalyst, suggesting the formation of stable carbon support for hosting the active sites. The HAADF-STEM images obtained in different areas in **Fig. 4**G and **4**H also affirmed the uniformly distributed single metal atoms. The co-existence of the Fe and N sites detected by using EELS (**Fig. 4I)** strongly suggested the coordination of Fe with N.

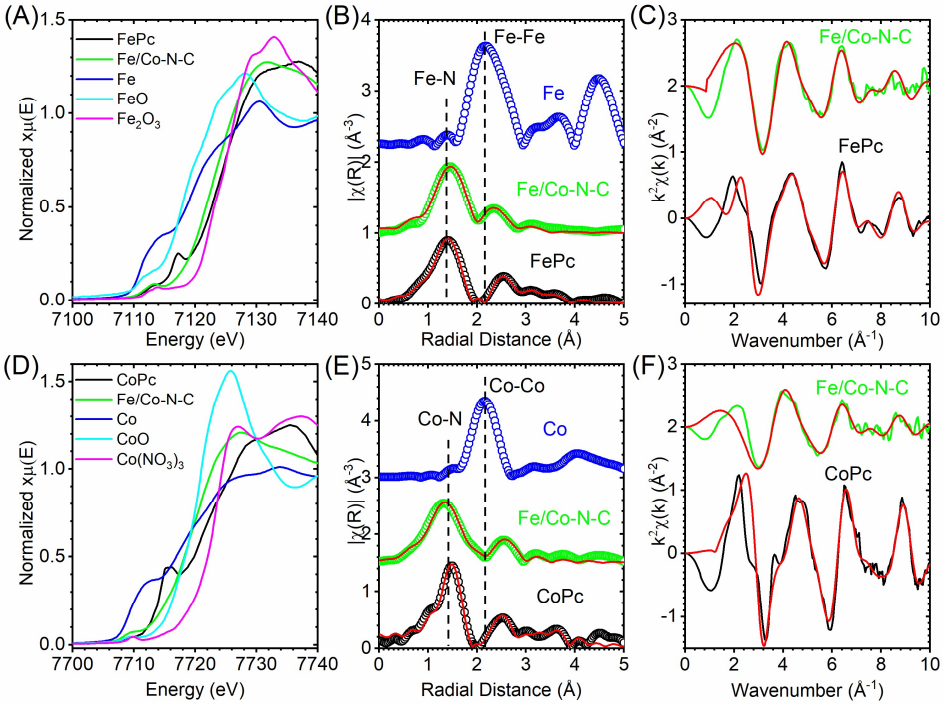

Fig. 5. (A-C) Fe K-edge XANES spectra, fit of the Fourier transform R-space EXAFS, and fit of k-space EXAFS (D-F) Co K-edge XANES spectra, fit of the Fourier transform R-space EXAFS, and fit of k-space EXAFS.

To further verify the local coordination environment of atomically dispersed Co and Fe sites in the Fe/Co-N-C catalyst,[48] the X-ray absorption spectroscopy (XAS) measurements[49] were conducted (**Fig. 5)**. The Fe K-edge X-ray absorption near edge structure (XANES) is adjacent to but on the left side of those of FePc and Fe_2O_3 reference, suggesting that the Fe oxidization state in the catalyst is close to FePc but lower than Fe^{3+} (**Fig. 5**A). Similarly, the Co K-edge XANES shows that the oxidization state of Co atoms in Fe/Co-N-C is close to Co^{2+}. The Fourier transformed extended X-ray absorption fine structure (EXAFS) spectra in *R*-space of Fe and Co (**Fig. 5**B and E) display a primary peak around 1.5Å, which standards for Fe-N/C and Co-N/C bonds, respectively. Comparing with Fe and Co metal foil, there is no apparent metal-metal scattering peak around 2.1Å for the Fe/Co-N-C catalyst, which indicates no Fe or Co metallic cluster formation. These results are consistent with STEM findings and confirm that both Fe and Co sites are atomically dispersed into the carbon matrix. Furthermore, the modeled EXAFS fitting (**Fig.** 5B, C, E, and F) also confirms that Fe and Co do not have any metal-metal bond. The EXAFS fitting results using FePc and CoPc as the standard models (Table S3 and 4) conclude that the average coordination number of Fe-N and Co are 3.9±0.7 and 4.6±1.2, respectively. Given the acceptable error bar, the XAS fitting analysis further confirms the formation of the well-defined CoN_4 and FeN_4 moieties in the Fe/Co-

Fe/Co-N-C catalysts for PEMFCs and DMFCs.

The rotating ring-disk electrode (RRDE) tests were firstly conducted for evaluating ORR activity of the Fe/Co-N-C catalyst in 0.5 M H_2SO_4 electrolyte. The best-performing Fe/Co-N-C catalyst was optimized by adjusting the precursor feeding ratio of Zn/Co in the first chemical Co doping step and the content of Fe ions used for the second adsorption step. Fig. 6A indicates that the optimized Zn/Co precursor feeding ratio was 11/2. Excessive Co-doping with Zn/Co ratio up to 9/4 may result in the formation of inactive Co-based metal species, as displayed in **Fig. S12**. The atomically dispersed Fe-N-C (13:0) catalyst with a similar size was synthesized through identical procedures except for the pre-doping of Co-atoms at the first step for a comparison. The ORR polarization curves of Fe-N-C catalysts was almost overlapped with the optimal Fe/Co-N-C catalyst in the kinetically-controlled potential range (Fig. 6A), suggesting no synergy between CoN_4 and FeN_4 sites. However, the larger limiting current of the Fe/Co-N-C catalyst reflected that it possesses a higher surface area and better mass transfer than that of the Fe-N-C catalyst without Co-doping. Through adjusting the content of Fe ion precursor (*i.e.*, 3.5 mg $FeCl_3$), the Fe/Co-N-C catalyst achieved an $E_{1/2}$ of 0.85 V *vs.* RHE at a catalyst loading of 0.6 mg cm^{-2} in 0.5 M H_2SO_4 electrolyte with a rotation speed of 900 rpm (**Fig. 6**B). Similarly, the

low amount of Fe leads to an insufficient number of active sites. In contrast, the excessive ones cause the formation of inactive Fe

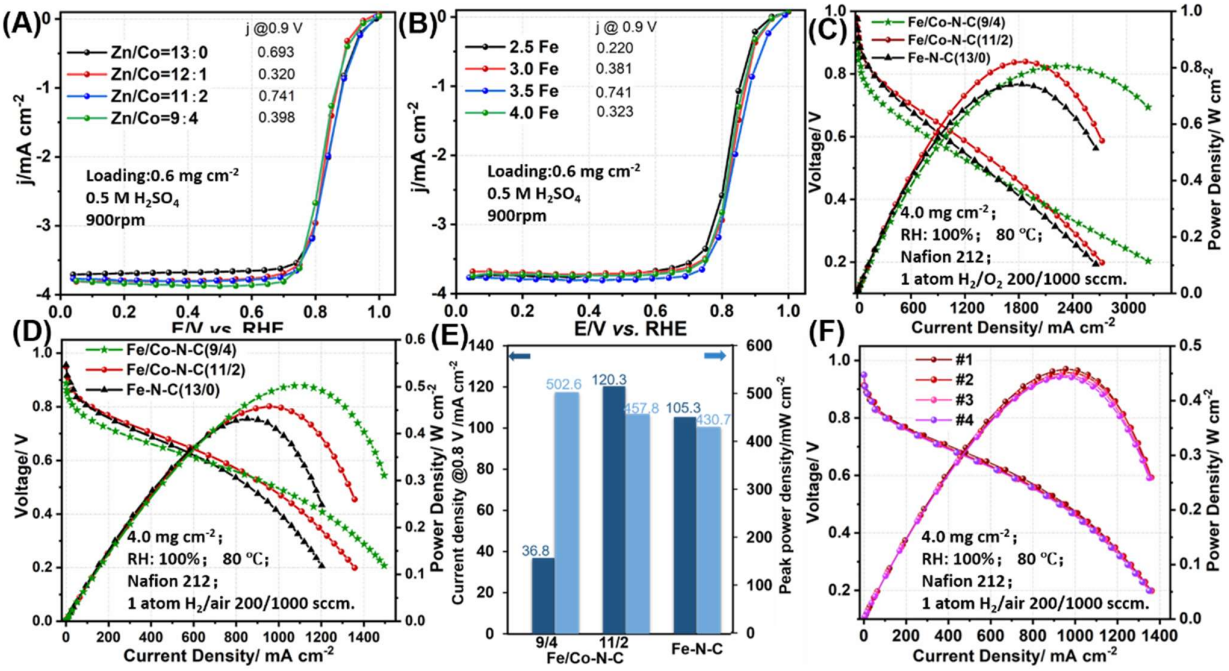

Fig. 6. ORR polarization plots of Fe/Co-N-C catalysts (A) with constant Fe feeding does (3.5Fe) and different Co-doping ratio, and (B) with constant Co-doping ratio (11/2) and different Fe adsorption content. Polarization plots of (C) H_2-O_2 cell and (D) H_2-air cell using Fe/Co-N-C catalysts and Fe-N-C catalysts, respectively. (E) Comparison of the current density at 0.8 V and peak power density of the catalysts in the H_2-air fuel cell. (F) The performance degradation within four times of continuous scanning.

nanoclusters, which cause adverse ORR activity. The optimized Fe/Co-N-C catalysts outperformed the previously ever-reported Fe/Co-N-C catalysts[38] and comparable to most of the Fe-N-C catalysts.[14] The density of active sites could be quantified by the CO-stripping[50, 51] and nitrite reduction stripping method.[52] Here we conducted the nitrite stripping experiment for evidencing the increased number of the active site in the Fe/Co-N-C (11/2) catalyst. Based on the CV curves in **Fig. S13**, the as-calculated gravimetric site density for Fe/Co-N-C is around 17.8 μmol g^{-1}, which is higher than that of Fe-N-C (11.2 μmol g^{-1}). The effective removal of Zn atoms, due to the pre-doping of Co, created more N-coordinated defects for the subsequent Fe adsorption, leading to an increased density of FeN_4 active sites accessible to reactants.

Aside from the improved catalytic activity in the acidic electrolyte, the Fe/Co-N-C catalyst also demonstrated excellent stability with only 20 mV $E_{1/2}$ shift after 10,000 potential cycling test between 0.6 V-1.0 V, shown in **Fig. S14**A. Besides, Fe/Co-N-C catalysts retained up to 80% of its initial current density after a 15-hour chronoamperometry test at 0.83 V (Fig. S14B). Although stability tests may not be long enough, most of the activity loss of M-N-C catalysts occurs at the initial stage during the ORR. We did not identify the increased degree of graphitization of the carbon between ZIF-8 derived N-C and Co-N-C catalysts. Thus, it remains a puzzle to clearly explain why the Fe/Co-N-C catalyst is more stable than Fe-N-C. However, we always observed enhanced stability of Co-N-C relative to Fe-N-C catalysts.[11] The enhanced stability is probably benefited from the intrinsically stable CoN_4 sites.[34] To determine the importance of the sequence to introduce Co and Fe in the catalyst, we designed a controlled experiment to synthesize a Co/Fe-N-C catalyst by pre-doping Fe first into ZIF-8 precursor and then adsorption Co ions at the second step, followed by identical heating procedures. The morphology and size are similar to Fe/Co-N-C (**Fig. S15A**). However, the Co/Fe-N-C catalyst is inferior to the regular Fe/Co-N-C catalyst (pre-doped Co and then adsorbed Fe ions second) (**Fig. S15B**). The comparison further highlights the significance of pre-doping Co at the first step is critical for enhancing the catalyst performance of the dual-site Fe/Co-N-C catalyst.

Two Fe/Co-N-C catalysts (with Zn/Co ratios of 9/4 and 11/2) were selected for further MEA studied in both H_2-oxygen/air and methanol-air fuel cells. The aim of studying the H_2-oxygen/air cells is to investigate the actual ORR activity Fe/Co-N-C catalysts in MEA with enhanced mass transport. Also, based on the baseline performance of MEAs under H_2-air conditions, we can determine the possible polarization loss at the anode in DMFCs due to the sluggish MOR. **Fig. 6**C presents H_2-O_2 cell performance for two Fe/Co-N-C (9/4 and 11/2) catalyst and the Fe-N-C(13/0) catalyst.

ARTICLE

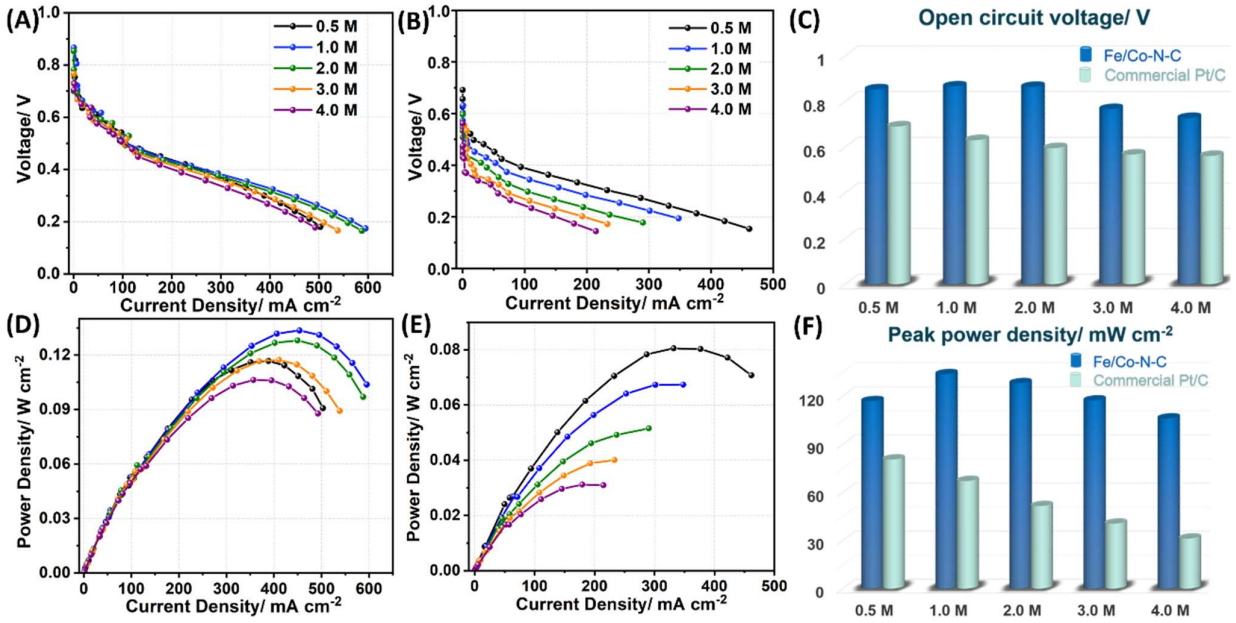

Fig 7. Polarization plots of (A and B) cell voltage and (D and E) power density versus current density of methanol-air cell using Fe/Co-N-C (11/2) (A and D) and commercial Pt/C (B and E) as cathode catalysts as a function of methanol concentration. (C) OCV and (F) peak power density of the Fe/Co-N-C(11/2) and commercial Pt/C catalysts used as cathode catalysts in the methanol-air cell. Anode: 4.0 mg cm^{-2} PtRu/C; cathode: 5.0 mg cm^{-2} Fe/Co-N-C(11/2) or 0.9 mg cm^{-2} Pt/C; 0.5 mL min^{-1} methanol flow rate; 1.0 atm air 1000 mLmin^{-1} flow rate; membrane: Nafion 212; cell: 80 °C.

Both Fe/Co-N-C catalysts conveyed higher power densities of 800 mW cm^{-2} when compared to the Fe-N-C catalyst (740 mW cm^{-2}). In the whole voltage range, the Fe/Co-N-C (11/2) catalyst performs better than the single site Fe-N-C catalyst, further confirming enhanced catalytic activity by using the dual-site Co and Fe, relative to individual Fe. Then MEA performance under more practical H_2-air conditions was assessed, and the corresponding VI polarization plots are shown in **Fig. 6D**. Two performance metrics, including the current density at 0.8 V and peak power densities, were summarized in **Fig.6E** for the studied three catalysts. The power density of the MEA with the Fe/Co-N-C (9/4) catalyst reached 502 mW cm^{-2}, while the value decreased to 458 mW cm^{-2} as the Co-doping content reduced to 11/2. Both these values are significantly higher than most of the current M-N-C PGM-free cathodes **(Table S2)**.[14, 18, 38, 53-56] Although achieving a slightly lower power density relative to the Fe/Co-N-C (9/4), the Fe/Co-N-C (11/2) with optimized Co-content exhibited the highest current density of 120.3 mA cm^{-2} at 0.8 V, which is approaching to U.S. DOE target (150 mA cm^{-2}). Even though the Fe-N-C (13:0) catalyst possesses similar intrinsic activity with Fe/Co-N-C (11/2) in the RDE test, it conveys inferior performance in both kinetic region and mass transport under H_2-air conditions. The reason could be attributed to a higher Brunauer-Emmett-Teller (BET) surface area and a larger extent of mesopores in Fe/Co-N-C catalysts (807.6 m^2/g) than that in Fe-N-C catalysts (620.7 m^2/g), as evidenced in the nitrogen adsorption-desorption isotherm curves and pore distribution plots displayed in **Fig. S16**. Thus, the pre-doping of Co is beneficial for creating significant mesopores and favoring the O_2 diffusion to a larger number of FeN_4 sites within the thick 3D cathode. These results further highlighted the importance of catalysts structure and porosity in optimizing MEA performance, which has more complex conditions than the simple RDE test in aqueous electrolytes. Importantly, the Fe/Co-N-C (11/2) catalyst maintained the performance with negligible variation during four times continuous test (**Fig. 6**F), manifesting its considerable stability possibly.

Inspired by the remarkably enhanced MEA performance in H_2-air cells as well as the intrinsic methanol tolerance of M-N-C catalysts, the best performing Fe/Co-N-C catalyst was studied in a methanol-air cell with a series of methanol feeding concentrations. **Fig. 7**A and **7**B present the polarization plots of DMFCs by using both the Fe/Co-N-C (11/2) and commercial Pt/C cathode. Polarization plots at the same methanol concentration were continuously

recorded twice (**Fig. S17**). This is to verify that the performance difference is caused by the methanol feeding concentrations rather than catalyst activity decay. Their open-circuit voltage (OCV) under different methanol concentrations were compared in **Fig. 7**C. The MEA using the Fe/Co-N-C catalyst achieved an OCV of 0.87 V at 1.0 M methanol at the anode. When the methanol concentration is increased from 0.5 to 2.0 M, the corresponding OCVs and performance of MEAs remained nearly unchanged. A higher concentration of methanol beyond 3.0 M results in a slight performance decrease, especially in the mass transport region (**Fig. 7**D). In contrast, the OCV of the MEA using the Pt/C cathode only reached 0.7 V, implying a significant voltage loss due to the mixed potential from the ORR and the MOR at the cathode (**Fig. 7B**). Also, with an increase of methanol concentration, OCVs and MEA performance of the Pt/C cathode suffer from a continuous and rapid drop (Fig. 7B and 7E). The measured power densities of these two MEAs using Fe/Co-N-C and Pt/C cathodes were compared in **Fig. 7F**. The maximum peak power density of 135 $mWcm^{-2}$ was achieved at 1.0 M for the Fe/Co-N-C (11/2) cathode, but slightly decreases at higher concentration (*e.g.*, 106 mW cm^{-2} at 4.0 M). In contrast, the peak power density of the Pt/C cathode experienced a severe degradation as the methanol concentration increased from 0.5 M (80 $mWcm^{-2}$) to 4.0 M (31 $mWcm^{-2}$). The comparison validates an excellent methanol tolerance of the Fe/Co-N-C catalyst in DMFCs. However, it should be noted that there is still noticeable performance degradation in the mass transfer region for the Fe/Co-N-C cathode. As we fundamentally elucidated by using RDE tests, both FeN_4 and CoN_4 sites are not complete methanol tolerance. They still suffer from ORR activity loss in aqueous electrolytes due to methanol adsorption, especially during the high potentials for the ORR. Also, the effects of methanol on proton conductivity and O_2 diffusion rates within ionomers may cause performance degradation of MEAs.[39, 40, 57] Besides, excessive methanol may generate water flooding issues.[57, 58] However, compared to traditional Pt/C cathodes, the degradation in the mass transfer region is significantly alleviated by using the Fe/Co-N-C cathode. The performance of a Fe-N-C catalyst was also studied in a methanol-air cell. The Fe-N-C catalyst delivered a much lower peak power density of 124 mW cm^{-2} (**Fig. S18)**, which is lower than the optimal Fe/Co-N-C (135 mW cm^{-2}). This further confirms that the optimal Fe/Co-N-C catalyst, which has favorable porosity and morphology for improved mass transport, is superior to single-site Fe-N-C catalysts in DMFCs.

When comparing to all reported DMFC performance, the achieved peak power density in this work is the highest by using a PGM-free cathode (**Fig. S19**).[6, 9, 59-62] The encouraging performance may be due to multiple factors, including the enhanced intrinsic ORR activity of the atomically dispersed FeN_4 and CoN_4 sites, outstanding methanol tolerance ability of PGM-free MN_4 sites, and the improved mass transport from favorable mesopores in catalysts. Therefore, the atomically dispersed metal site catalyst would hold a great promise for viable applications in DMFCs and other direct fuel *(e.g.*, ethanol and NH_3) fuel cells with enhanced performance and durability.

Conclusions

In summary, atomically dispersed single metal site M-N-C catalysts demonstrated a great promise to be high-performance PGM-free cathodes for DMFCs. At first, using a model Fe-N-C catalyst containing exclusive FeN_4 active sites, we experimentally studied its ORR behavior as a function of methanol concentration. When methanol concentration is lower than 2.0 M, the effect of methanol on the ORR is negligible. Higher methanol concentrations over 4.0 M cause a noticeable irreversible decay in ORR activity due to the possible strong adsorption of methanol, especially during an electrochemical environment. Combined with DFT calculation, we further elucidated that FeN_4 moieties have relatively weaker methanol adsorption when compared to pyridinic N, CoN_4, and MnN_4 active sites. Adsorption of methanol on pyridinic N is independent of applied potential. In contrast, the adsorption on MN_4 sites is dependent mainly on electrode potentials and becomes stronger at higher applied potentials. However, the methanol adsorption does not affect the $4e^-$ ORR pathway and destroy the structure of the FeN_4 moiety.

Due to the excellent methanol tolerance of Fe-N-C catalysts, we rationally designed an atomically dispersed dual-site Fe/Co-N-C catalyst via a two-step synthesis approach combining chemical Co-doping into ZIF-8 and the subsequent Fe ion adsorption, along with a separated heating treatment after each step. Instead of the possible synergy between Fe and Co, we discovered that the pre-doping Co at the first step is crucial for adjusting the porosity of the carbon host and enhancing catalyst stability. The Fe/Co-N-C catalyst with optimal metal precursor content exclusively contains atomically dispersed FeN_4 and CoN_4 sites. As a result, the Fe/Co-N-C catalyst exhibited outstanding ORR activity and stability in the acidic electrolyte with $E_{1/2}$ reached 0.85 V. Furthermore, the MEA by using the Fe/Co-N-C cathode delivered remarkable power density up to 502 and 135 mW cm^{-2} using 1.0 bar H_2/air and 1.0 M methanol, respectively. Unlike the significant performance loss of traditional Pt/C cathode, the Fe/Co-N-C cathode has enhanced methanol tolerance in DMFCs at the studied methanol concentrations up to 4.0 M. The MEA studies further verified that the pre-chemical doping of Co atoms is the key for the generation of mesopores, which are pivotal in promoting the mass transfer and maximizing the accessibility of FeN_4 active sites in the cathode. The finely devised Fe/Co-N-C catalysts afforded a promising approach to engineering M-N-C catalysts with exceptional methanol tolerance ability and enhanced power output.

Currently, the performance gap between the H_2-air and the methanol-air cells is still significant for M-N-C cathode catalysts. It is due to various factors, including the insufficient anode catalytic activity, methanol poisoning on MN_4 active sites, and additional mass/charge transport resistance resulting from methanol within the cathode. Therefore, further efforts are demanded to boost M-N-C cathode performance in DMFCs through the increasing density of the active site, engineering the porosity with uniform ionomer dispersion, and optimizing carbon structures for improved mass transport.

Conflicts of interest

There are no conflicts to declare.

Acknowledgments

The authors acknowledge the financial support from the U.S. Department of Energy, Office of Energy Efficiency and Renewable Energy (EERE), Fuel Cell Technology Office (DE-EE0008075, DE-EE0008076, and DE-EE0008417) along with National Science Foundation (CBET-1604392, 1804326). This research used resources of the beamline 12-BM of the Advanced Photon Source (APS), a U.S. Department of Energy (DOE) Office of Science User Facility operated for the DOE Office of Science by Argonne National Laboratory under Contract DE-AC02-06CH11357.

Notes and references

1. Z. Qiao, S. Hwang, X. Li, C. Wang, W. Samarakoon, S. Karakalos, D. Li, M. Chen, Y. He, M. Wang, Z. Liu, G. Wang, H. Zhou, Z. Feng, D. Su, J. S. Spendelow and G. Wu, *Energy Environ. Sci.*, 2019, **12**, 2830-2841.
2. S. Zhu, J. Ge, C. Liu and W. Xing, *EnergyChem*, 2019, **1**, 100018.
3. Y. Li, H. Wang, C. Priest, S. Li, P. Xu and G. Wu, *Adv. Mater.*, 2020, **10.1002/adma.202000381**, 2000381.
4. X. X. Wang, M. T. Swihart and G. Wu, *Nat. Catal.*, 2019, **2**, 578-589.
5. X. Zhao, M. Yin, L. Ma, L. Liang, C. P. Liu, J. H. Liao, T. H. Lu and W. Xing, *Energy Environ. Sci.*, 2011, **4**, 2736-2753.
6. Q. Li, T. Y. Wang, D. Havas, H. G. Zhang, P. Xu, J. T. Han, J. Cho and G. Wu, *Adv. Sci.*, 2016, **3**, 1600140.
7. D. Sebastian, A. Serov, I. Matanovic, K. Artyushkova, P. Atanassov, A. S. Arico and V. Baglio, *Nano Energy*, 2017, **34**, 195-204.
8. X. Xu, Z. Xia, X. Zhang, H. Li, S. Wang and G. Sun, *Nanoscale*, 2020.
9. Z. Xia, X. Xu, X. Zhang, H. Li, S. Wang and G. Sun, *J. Mater. Chem. A*, 2020, **8**, 1113-1119.
10. J. Hou, M. Yang, C. Ke, G. Wei, C. Priest, Z. Qiao, G. Wu and J. Zhang, *EnergyChem*, 2020, **2**, 100023.
11. X. X. Wang, V. Prabhakaran, Y. He, Y. Shao and G. Wu, *Adv. Mater.*, 2019, **31**, 1805126.
12. Q. Shi, S. Hwang, H. Yang, F. Ismail, D. Su, D. Higgins and G. Wu, *Mater. Today*, 2020, DOI: doi.org/10.1016/j.mattod.2020.02.019.
13. J. Li, M. Chen, D. A. Cullen, S. Hwang, M. Wang, B. Li, K. Liu, S. Karakalos, M. Lucero, H. Zhang, C. Lei, H. Xu, G. E. Sterbinsky, Z. Feng, D. Su, K. L. More, G. Wang, Z. Wang and G. Wu, *Nat. Catal.*, 2018, **1**, 935-945.
14. J. Li, H. Zhang, W. Samarakoon, W. Shan, D. A. Cullen, S. Karakalos, M. Chen, D. Gu, K. L. More, G. Wang, Z. Feng, Z. Wang and G. Wu, *Angew. Chem. Int. Ed.*, 2019, **58**, 18971-18980.
15. H. G. Zhang, S. Hwang, M. Y. Wang, Z. X. Feng, S. Karakalos, L. L. Luo, Z. Qiao, X. H. Xie, C. M. Wang, D. Su, Y. Y. Shao and G. Wu, *J. Am. Chem. Soc.*, 2017, **139**, 14143-14149.
16. Y. He, S. Hwang, D. A. Cullen, M. A. Uddin, L. Langhorst, B. Li, S. Karakalos, A. J. Kropf, E. C. Wegener, J. Sokolowski, M. Chen, D. Myers, D. Su, K. L. More, G. Wang, S. Litster and G. Wu, *Energy Environ. Sci.*, 2019, **12**, 250-260.
17. G. Zhang, X. Yang, M. Dubois, M. Herraiz, R. Chenitz, M. Lefèvre, M. Cherif, F. Vidal, V. P. Glibin, S. Sun and J.-P. Dodelet, *Energy Environ. Sci.*, 2019, **12**, 3015-3037.
18. Q. Shi, C. Zhu, D. Du and Y. Lin, *Chem. Soc. Rev.*, 2019, **48**, 3181-3192.
19. G. Wu, K. L. More, C. M. Johnston and P. Zelenay, *Science*, 2011, **332**, 443-447.
20. M. Xiao, H. Zhang, Y. Chen, J. Zhu, L. Gao, Z. Jin, J. Ge, Z. Jiang, S. Chen, C. Liu and W. Xing, *Nano Energy*, 2018, **46**, 396-403.
21. M. Chen, Y. He, J. S. Spendelow and G. Wu, *ACS Energy Lett.*, 2019, **4**, 1619-1633.
22. D. Sebastián, V. Baglio, A. S. Aricò, A. Serov and P. Atanassov, *Appl. Catal. B: Environ.*, 2016, **182**, 297-305.
23. L. Yang, D. Cheng, H. Xu, X. Zeng, X. Wan, J. Shui, Z. Xiang and D. Cao, *Proc. Natl. Acad. Sci. U S A*, 2018, **115**, 6626-6631.
24. B. You, N. Jiang, M. Sheng, W. S. Drisdell, J. Yano and Y. Sun, *ACS Catal.*, 2015, **5**, 7068-7076.
25. Y. Ma, S. Luo, M. Tian, J. E. Lu, Y. Peng, C. Desmond, Q. Liu, Q. Li, Y. Min and Q. Xu, *J. Power Sources*, 2020, **450**, 227659.
26. S. Mukherjee, X. Yang, W. Shan, W. Samarakoon, S. Karakalos, D. A. Cullen, K. More, M. Wang, Z. Feng, G. Wang and G. Wu, *Small Methods*, 2020, **4**, 1900821.
27. C. Zhu, S. Fu, Q. Shi, D. Du and Y. Lin, *Angew. Chem. Int. Ed.*, 2017, **56**, 13944-13960.
28. A. Zitolo, V. Goellner, V. Armel, M.-T. Sougrati, T. Mineva, L. Stievano, E. Fonda and F. Jaouen, *Nat. Mater.*, 2015, **14**, 937-942.
29. T. Asset and P. Atanassov, *Joule*, 2020, **4**, 33-44.
30. J.-C. Li, S. Maurya, Y. S. Kim, T. Li, L. Wang, Q. Shi, D. Liu, S. Feng, Y. Lin and M. Shao, *ACS Catal.*, 2020, **10**, 2452-2458.
31. J.-C. Li, F. Xiao, H. Zhong, T. Li, M. Xu, L. Ma, M. Cheng, D. Liu, S. Feng, Q. Shi, H.-M. Cheng, C. Liu, D. Du, S. P. Beckman, X. Pan, Y. Lin and M. Shao, *ACS Catal.*, 2019, **9**, 5929-5934.
32. Y. Mun, S. Lee, K. Kim, S. Kim, S. Lee, J. W. Han and J. Lee, *J. Am. Chem. Soc.*, 2019, **141**, 6254-6262.
33. R. Jiang, L. Li, T. Sheng, G. Hu, Y. Chen and L. Wang, *J. Am. Chem. Soc.*, 2018, **140**, 11594-11598.
34. Y. Shao, J. P. Dodelet, G. Wu and P. Zelenay, *Adv. Mater.*, 2019, **31**, 1807615.
35. Y. He, Liu, Shengwen, Priest, Cameron, Shi, Qiurong, Wu, Gang *Chem. Soc. Rev.*, 2020, **49**, 3484-3524.
36. H. Zhang, H. T. Chung, D. A. Cullen, S. Wagner, U. I. Kramm, K. L. More, P. Zelenay and G. Wu, *Energy Environ. Sci.*, 2019, **12**, 2548-2558.
37. Y. Zhu, J. Sokolowski, X. Song, Y. He, Y. Mei and G. Wu, *Adv. Energy Mater.*, 2020, **10**, 1902844.
38. J. Wang, Z. Huang, W. Liu, C. Chang, H. Tang, Z. Li, W. Chen, C. Jia, T. Yao and S. Wei, *J. Am. Chem. Soc.*, 2017, **139**, 17281-17284.
39. A. L. Ocampo, R. H. Castellanos and P. J. Sebastian, *J. New Mater. Electrochem. Syst.*, 2002, **5**, 163-168.
40. R. N. Itoe, G. D. Wesson and E. E. Kalu, *J. Electrochem. Soc.*, 2000, **147**, 2445-2450.
41. I. Martinaiou, A. H. M. Videla, N. Weidler, M. Kübler, W. D. Z. Wallace, S. Paul, S. Wagner, A. Shahraei, R. W. Stark and S. Specchia, *Appl. Catal. B: Environ.*, 2020, **262**, 118217.
42. C. Zhu, Q. Shi, B. Z. Xu, S. Fu, G. Wan, C. Yang, S. Yao, J. Song, H. Zhou and D. Du, *Adv. Energy Mater.*, 2018, **8**, 1801956.
43. D. Kim, J. Shi and Y. Liu, *J. Am. Chem. Soc.*, 2018, **140**, 9127-9131.

44. X. Zhao and Y. Liu, *J. Am. Chem. Soc.*, 2020, **142**, 5773-5777.
45. X. Zhao, J. Shi, Y. Ji and Y. Liu, *WIREs Comput. Mol. Sci.*, 2019, **9**, e1418.
46. A. Uddin, L. Dunsmore, H. Zhang, L. Hu, G. Wu and S. Litster, *ACS Appl. Mater. Interfaces*, 2020, **12**, 2216-2224.
47. M. Knez, R. Scholz, K. Nielsch, E. Pippel, D. Hesse, M. Zacharias and U. Gösele, *Nat. Mater.*, 2006, **5**, 627-631.
48. M. Wang, L. Árnadóttir, Z. J. Xu and Z. Feng, *Nano-Micro Lett.*, 2019, **11**, 47.
49. Z. Feng, Q. Ma, J. Lu, H. Feng, J. Elam, P. C. Stair and M. J. Bedzyk, *RSC Adv.*, 2015, **5**, 103834-103840.
50. F. Luo, A. Roy, L. Silvioli, D. A. Cullen, A. Zitolo, M. T. Sougrati, I. C. Oguz, T. Mineva, D. Teschner, S. Wagner, J. Wen, F. Dionigi, U. I. Kramm, J. Rossmeisl, F. Jaouen and P. Strasser, *Nat. Mater.*, 2020, 1-9.
51. N. R. Sahraie, U. I. Kramm, J. Steinberg, Y. Zhang, A. Thomas, T. Reier, J.-P. Paraknowitsch and P. Strasser, *Nat. Commun.*, 2015, **6**, 1-9.
52. M. Primbs, Y. Sun, A. Roy, D. Malko, A. Mehmood, M.-T. Sougrati, P.-Y. Blanchard, G. Granozzi, T. Kosmala and G. Daniel, *Energy Environ. Sci.*, 2020.
53. X. X. Wang, D. A. Cullen, Y. T. Pan, S. Hwang, M. Wang, Z. Feng, J. Wang, M. H. Engelhard, H. Zhang, Y. He, Y. Shao, D. Su, K. L. More, J. S. Spendelow and G. Wu, *Adv. Mater.*, 2018, **30**, 1706758.
54. X. Fu, P. Zamani, J. Y. Choi, F. M. Hassan, G. Jiang, D. C. Higgins, Y. Zhang, M. A. Hoque and Z. Chen, *Adv. Mater.*, 2017, **29**, 1604456.
55. H. T. Chung, D. A. Cullen, D. Higgins, B. T. Sneed, E. F. Holby, K. L. More and P. Zelenay, *Science*, 2017, **357**, 479-484.
56. X. Fu, F. M. Hassan, P. Zamani, G. Jiang, D. C. Higgins, J.-Y. Choi, X. Wang, P. Xu, Y. Liu and Z. Chen, *Nano Energy*, 2017, **42**, 249-256.
57. D. Sebastián, A. Serov, K. Artyushkova, J. Gordon, P. Atanassov, A. S. Aricò and V. Baglio, *ChemSusChem*, 2016, **9**, 1986-1995.
58. A. H. M. Videla, D. Sebastián, N. S. Vasile, L. Osmieri, A. S. Aricò, V. Baglio and S. Specchia, *Int. J. Hydrogen energy*, 2016, **41**, 22605-22618.
59. A. L. M. Reddy, N. Rajalakshmi and S. Ramaprabhu, *Carbon*, 2008, **46**, 2-11.
60. X. Xu, Z. Xia, X. Zhang, R. Sun, X. Sun, H. Li, C. Wu, J. Wang, S. Wang and G. Sun, *Appl. Catal. B: Environ.*, 2019, **259**, 118042.
61. Y.-C. Wang, L. Huang, P. Zhang, Y.-T. Qiu, T. Sheng, Z.-Y. Zhou, G. Wang, J.-G. Liu, M. Rauf and Z.-Q. Gu, *ACS Energy Lett.*, 2017, **2**, 645-650.
62. Y. He, Q. Tan, L. Lu, J. Sokolowski and G. Wu, *Electrochem. Energy Rev.*, 2019, **2**, 231-251.

Broader context

Hydrogen proton-exchange membrane fuel cells (PEMFCs) and direct methanol fuel cells (DMFCs), which both use low-temperature acidic PEMs as electrolytes, are promising power sources for a variety of application from portable electronics to electric vehicles. The development of high-performance platinum group metal (PGM)-free catalysts is highly demanded to address the high-cost issue of PEMFCs. Among studied PGM-free formulations, atomically dispersed M-N-C (M: Fe, Co, or Mn) catalysts have exhibited encouraging catalytic activity and stability for the oxygen reduction reaction (ORR). Importantly they have superior methanol tolerance during the ORR when compared to traditional Pt catalysts, which is ideal for the ORR cathode in DMFCs. This work provided an insightful understanding of methanol adsorption behavior on these PGM-free CN_x and MN_4 sites for rational catalyst design to improve DMFC performance. As a result, an innovative dual-site Fe/Co-N-C catalyst with an increased density of active sites and favorable porosity achieved exceptional power densities in both H_2- and methanol-air cells. Beyond H_2, this work demonstrated the excellent feasibility of using the atomically dispersed M-N-C catalysts for direct alcohol fuel cells.

TOC